Supporting Information

Molecular Assembly of Carbon Nitride-Based Composite Membrane for Photocatalytic Sterilization and Wound Healing

Xiaoxiao Peng,‡[a] Jin Ma,‡[a] Zhixin Zhou,[a] Hong Yang,[a] Jingjing Chen,[a] Ran Chen,[a] Kaiqing Wu,[a] Guangcheng Xi,[c] Songqin Liu,[a] Yanfei Shen[*b] and Yuanjian Zhang[*a]

[a] Jiangsu Engineering Laboratory of Smart Carbon-Rich Materials and Device, Jiangsu Province Hi-Tech Key Laboratory for Bio-Medical Research, School of Chemistry and Chemical Engineering, Southeast University, Nanjing, 211189, China, E-mail: Yuanjian.Zhang@seu.edu.cn

[b] Medical School, Southeast University, Nanjing, 210009, China, E-mail: Yanfei.Shen@seu.edu.cn

[c] Institute of Industrial and Consumer Product Safety, Chinese Academy of Inspection and Quarantine, Beijing, 100176, China

Table of Contents

Experiments

Materials.

Dicyandiamide (DCDA, 99%), 1-pyrroline N-oxide (DMPO) and 3,3',5,5'-tetramethylbenzidine (TMB) were purchased from Sigma-Aldrich, USA. Polyphosphoric acid (PPA, $P_2O_5\% \geq 85\%$), phosphoric acid (PA, GR, $\geq$ 85 wt.% in H_2O), 1-(4-Sulfobutyl)pyridin-1-ium Trifluoromethanesulfonate ($BSO_3Py^+\text{-}CF_3SO_3^-$, $\geq$ 97%) and peroxidase (HRP, from horseradish, $\geq$ 250 units/mg, solid) were purchased from Shanghai Macklin Biochemical Co., Ltd., China. Methanol (CH_3OH, AR) was purchased from Sinopharm Chemical Reagent Co., Ltd., China. Carbon nanotubes (CNTs, Table S4) were obtained from Chengdu Organic Chemicals Co. Ltd., China. Mannitol (Ultrapure), Superoxide dismutase (SOD, BR) and Ethylene diamine tetraacetic acid (EDTA, AR) were purchased from Aladdin, Shanghai yuanye and Titan, China, respectively. 2-(2-methoxy-4-nitrophenyl)-3-(4-nitrophenyl)-5-(2,4-disulfophenyl)-2H-tetrazolium (WST-8) was purchased from Beyotime Biotech. Co. Ltd., China. All dyes were purchased from Shanghai Macklin Biochemical Co., Ltd., China and used without further purification. E. *coli* [CMCC(B)44102] and S. *aureus* [CMCC(B)26003] (Shanghai Luwei Technology Co., Ltd., China) were selected as bacterial strains. H&E (hematoxylin-eosin staining), Masson and CD31 (Platelet endothelial cell adhesion molecule-1, PECAM-1/CD31) dye liquor sets were obtained from Servicebio, China. Ultrapure water (18.2 MΩ cm) was obtained from a Direct-Q 3 UV pure water purification system (Millipore, USA).

Characterization.

The X-ray diffraction (XRD) patterns were recorded by Ultima IV (Rigaku, Japan) with high-intensity Cu-Kα radiation (λ=1.54178 Å). The Fourier transform infrared (FT-IR) spectra were carried out on a Nicolet iS10 FT-IR spectrometer (Thermo, USA). The X-ray photoelectron spectrum (XPS) was measured by using ESCALAB 250Xi electron spectrometer (Thermo Fisher, USA) with the peak of C_{ls} (288.3 eV) as the reference for calibration. UV-vis absorbance spectra were obtained from Cary 100 (Agilent, Singapore) using a diffuse reflectance accessory with $BaSO_4$ as the reference sample (100% reflectance). The photoluminescence (PL) spectra were collected with a FluoroMax-4 spectrometer (Horiba, Japan). The zeta potential and dynamic light scattering (DLS) particle size distribution were obtained from Omni zeta potential analyzer (Brookhaven Instruments Corporation, USA). The viscosity value was measured by NDJ-8S digital viscometer (LiChen, China). The scanning electron microscopy (SEM) images were obtained from FEI Inspect

F50 (Thermo Fisher, USA) and EDS spectra were carried out on the Thermo Scientific NORAN System 7. The transmission electron microscopy (TEM) images were obtained from a Talos F200X transmission electron microscopy (Thermo Fisher, USA) at 200 kV accelerating voltage. Raman spectra were measured by using a DXRTM 3 Raman microscope (λ = 532 nm, Thermo Fisher, USA). The photoelectrochemical tests were measured on a CHI-600E electrochemical workstation (Chenhua, China) with a 150 W Xe lamp (NBeT, China) as the light source. The combustion elemental analysis was investigated by a Vario MICRO Cube (Elementar, German). The tensile test of the membranes was performed on Exceed E42 Electromechanical Universal Testing Machine (MTS, China). Solid diffuse reflection was measured by Ocean Optics (QE Pro, China). The photothermal effect was given by the thermal imaging device (AnalyzIR FOTRIC 280, China). The electron paramagnetic resonance (EPR) spectra were obtained from an EMXPlus spectrometer (Bruker A300, Germany). The absorbance of cells was measured by microplate reader (Multiskan GO, Thermo, USA). The histologic analysis images were obtained from an ECLIPSE Ci-L biological microscope (Nikon, China)

Preparation of polymeric carbon nitride (pCN).

The bulk pCN was prepared by heating dicyandiamide in air of muffle furnace for 4 hours to 550 ℃ and holding for 4 hours. The obtained yellow product was ground into powder before use.[1]

Preparation of pCN-PPA solution.

Polyphosphoric acid (PPA, 85%P_2O_5) and phosphoric acid (H_3PO_4, PA, 85% wt.% in water) were mixed to prepare the acid mixture with 75% concentration of phosphorus pentoxide (P_2O_5). *Unless otherwise specified, the PPA solvent mentioned below was referred to PPA (75% P_2O_5).* The pCN-PPA solution was obtained by mechanical agitating the mixture of pCN (0-2500 mg) and PPA (50 mL) at 80-100 ℃.

Precipitated rpCN from pCN-PPA solution.

As CH_3OH was a poor solvent for pCN but dissolvable in PPA, to make pCN precipitate from PPA solution, 200 mL methanol (CH_3OH) was added to the pCN-PPA solution through a constant pressure drop funnel. The precipitate was washed several times using CH_3OH and H_2O until the dispersion was neutral. After that, it was dried and the as-obtained light-yellow powder was denoted as rpCN.

Preparation of pCN-PPA pastes.

The intermediates during the dissolution of pCN in PPA, pCN-PPA pastes, were prepared to understand the dissolution mechanism. 600 mg pCN powder was added PPA of different concentration (1 mL, 72% P_2O_5, 75% P_2O_5, 80% P_2O_5). The mixtures were heated in an oven at 80 ℃ for 0, 1, 3, and 24 hours to obtain pCN-PPA paste at different time.

Preparation of pCN-IL solution.

The pCN-IL solution was obtained by mixing pCN and ionic liquids (1 mg/mL) at 100 ℃. Different ionic liquids have various acidities and viscosities, leading to different degrees of dissolution for pCN.

Preparation of pCN/CNTs, pCN+CNTs, and CNTs membrane.

pCN and CNTs with the proportion of 2:1, 5:1, or 10:1 were added to PPA solvent (75%P_2O_5) and mixed evenly. Then, the mixtures were co-precipitated by using CH_3OH and washed several times until the dispersions were neutral. The pCN/CNTs membranes were prepared by vacuum suction filtration of the pCN/CNTs dispersion. To prepare pCN+CNTs membrane, pCN and CNTs were added in PPA and precipitated, respectively. After that, pCN and CNTs precipitates were mixed, dispersed in water, and filtered into the final pCN+CNTs membrane. Compared to the pCN/CNTs membrane, there was no compounding of pCN and CNTs in PPA. CNTs membrane was prepared by precipitating using CH_3OH and washing several times until the dispersions were neutral. After that, the CNTs dispersion was filtered into the final CNTs membrane.

Photocatalytic degradation of RhB.

Briefly, Rhodamine B (RhB, 20 mg/L) and pCN, rpCN, CNTs membrane or pCN/CNTs membrane (2 mg/mL), were added in a quartz tank (d = 3 cm, h = 3 cm, 10 mL). First, the suspension was stirred for 60 mins in dark to ensure the establishment of adsorption equilibrium. Then, the quartz tank was top-irradiated by a 300 W Xe lamp (CEL-HXUV300E, China) with a short-pass filter cutting off lights of wavelength less than 400 nm at the density of 100 mW/cm² at 25 ± 0.5 °C. 1 mL of suspension was extracted at certain time intervals and put back after detection. The suspension of pCN and rpCN powder were centrifuged before testing. The photocatalytic oxidation efficiency of RhB was analyzed on the UV-Vis spectrophotometer at 554 nm.

Photocatalytic sterilization activity of pCN/CNTs membrane.

Gram-negative *E. coli* and gram-positive *S. aureus* were used as model bacteria. All tubes and culture medium were sterilized in the autoclave before experiments. The bacterial cells were grown in nutrient broth at 37 °C in a shaking incubator (170 rpm) overnight. The pCN/CNTs membrane (thickness = 20 μm) was cut into small pieces and added into a container with bacteria solution (0.25 cm^2, about 0.6 mg/mL, carbon nitride on the membrane was about 0.3 mg/mL). It was irradiated by simulated sunlight (300 W Xe lamp, with a short-pass filter cutting off lights of wavelength less than 400 nm) at the density of 100 mW/cm^{-2}. 100 μL of the diluted bacterial solution was spread on the nutrient agar solid plates and the plates were cultured for 16-18 hours at 37 °C. The number of colony forming units (CFU) per mL in each plate was counted to evaluate the antibacterial effect of the membrane. Experiments performed in the absence of photocatalyst conducted as the light control. Photocatalytic sterilization activity of CNTs membrane and rpCN were compared in the same way.

Regrowth test of bacteria.

After photocatalytic sterilization experiments, 1 mL of solution was added to 1 mL of nutrient broth liquid medium. Then the mixture was incubated at 37 °C for 15 hours in a shaking incubator. The transmittance at 600 nm was monitored to reflect the regrowth ability of bacteria.

Photocatalytic stability of pCN/CNTs membrane.

Take *S. aureus* as an example, the bacterial cells were grown in nutrient broth at 37 °C in a shaking incubator (170 rpm) overnight. PCN/CNTs membrane was added into a container with bacteria solution (0.6 mg/mL). It was irradiated by simulated sunlight (300 W Xe lamp, with a short-pass filter cutting off lights of wavelength less than 400 nm) for 60 mins at the density of 100 mW/cm^2. 100 μL of the diluted bacterial solution was spread on the nutrient agar solid plates and the plates were cultured for 16-18 hours at 37 °C. The number of CFU/mL in each plate was counted to evaluate the antibacterial effect of the membrane. The pCN/CNTs membrane was washed by normal saline after each photocatalytic sterilization. These steps were repeated for more than twenty times.

Scavenger quenching experiments and EPR test for ROS.

The scavengers used were mannitol for hydroxyl radical (•OH), SOD for superoxide radical (•O$_2^-$), EDTA for hole. O$_2$ and Ar were purged into the solution to verify the presence of •O$_2^-$. To rule out the degradation caused by the RhB dye itself, the light source of 400 nm was used. The scavengers were added into dye solution of known concentration before illumination. The inhibition effect was evaluated by the change of absorbance after illumination with the addition of catalysts. The reactive oxygen species (ROS) that participated in the photoirradiation of pCN/CNTs membrane, pCN powder and rpCN powder were also investigated by the spin trapping-EPR tests at room temperature. DMPO was used as a spin trapping reagent to detect •O^{2-}. The measurements were conducted as follows: catalysts (1 mg) were dispersed in CH$_3$OH solution (500 μL) containing DMPO (0.1 mmol) with a 2 mL quartz bottle, which was sealed with a rubber septum cap. After short ultrasonication for 5 min, a Xe lamp (λ > 400 nm) was used as the light source. Samples were collected at different time intervals and filtrated by 0.22 μm membrane to exclude the influence of photocatalysts.

Comparative experiments of bacteriostatic cloth.

First, a piece of white cloth was positioned between two layers of black normal cloth or pCN/CNTs membrane to make a fully-covered sandwich shelter. Then, they were soaked in the sewage with *S. aureus* and irradiated under sunlight intermittently. The growth of bacteria on the white cloth was evaluated to reflect the bacteriostatic effect.

In vitro toxicity and safety study.

The in vitro cytotoxicity was measured by following a standard CCK-8 viability assay against 4T1 cells. Cells were seeded at a density of 15000 cells/well in 48-well plates and incubated overnight. Afterward, the cells were incubated with the pCN/CNTs membrane at different concentrations (0, 50, 100, 250 μg/mL) at 37 °C in a 5% CO$_2$ atmosphere for 24 h, respectively. The formulation was changed with the fresh 1640 medium containing 10% CCK-8 solution, and then the cells were incubated in the dark for 3 hours. The absorbance of cells was measured by using a microplate reader at 460 nm, and the relative viability (mean and SD, n = 3) was represented as test sample / control sample (untreated cells). Each sample was tested in triplicate. Untreated cells represented 100% viability.

In vivo therapeutic effect of the pCN/CNTs membrane on *S. aureus*-infected wounds.

The animal studies were approved by the Animal Care and Welfare Committee of Southeast University (20200327004). To study the antibacterial efficacy of the pCN/CNTs membrane in vivo on actual wounds, a series of animal experiments were designed. The healthy C57BL/6 (SPF) mice (6-8 weeks, male), bought from Qing Long Shan, Nanjing, were used as research models. A round full-thickness cutaneous wound with the diameter of 8mm was cut on the back of each mouse. To create *S. aureus*-infected wounds, 40 μL 1×10^6 CFU *S. aureus* solution was sprayed on each wound. For comparison, the mice were divided into two groups, which treated with the diameter of 8 mm pCN/CNTs membrane or the control gauze on the wounds. The mice walked together under sunlight for a few times every day. Five groups of mice were evaluated as parallel experiments.

Histological analysis.

After treating for 9 days, the mice were sacrificed. Then, tissues over the wound bed were removed and immersed in neutral formaldehyde. The tissues were put into melted paraffin and were sliced using microtome after cooling. The tissue slice was flattened biological tissue stall baking machine to stain, followed by incubating with H&E, Masson and CD31dye liquor sets. H&E, Masson and CD31 staining were used to investigate the inflammation response, collagen deposition and neovascularization in the wound area, respectively. Finally, the slice was dehydrated and sealed, the sections were observed under a biological microscope.

Computational method.

Adsorption models of $H_2O(HPO_3)_1$, $H_2O(HPO_3)_2$ and $H_2O(HPO_3)_3$ solvent molecules on pCN were explored by quantum chemical calculations. pCN nanosheet was modeled by a 5×5×5 trigonal 2-dimensional cluster to compromise the computational cost and accuracy. First, the 5×5×5 trigonal 2-dimensional pCN cluster and solvent molecules were separately optimized. Then, the three adsorbed systems of solvent molecules on pCN cluster were optimized. The adsorption energy ($E_{ads-molecule}$) was calculated by

$$E_{ads-molecule} = E_{CN+molecule} - E_{CN} - E_{molecule}$$

where $E_{CN+molecule}$ and E_{CN} are the total energies of the pCN cluster with and without adsorbed molecule, respectively. $E_{molecule}$ is the energy of the adsorbed molecule.

In the models before optimization, solvent molecules were placed in three positions bridge (B), top (T) and hollow (H), and the distance of solvent molecule was about 5 Å from pCN cluster. During the optimization process, the solvent molecules gradually moved to the H position, which proved the H position was the most stable adsorption site relative to the T and B positions, due to the

hydrogen atom from solvent molecules was subjected to the smallest repulsive force by pCN cluster. All equilibrium geometries were optimized by the density functional theory (DFT) with double hybrid M06-2X exchange-correlation functional and 6-31G(d,p) basis set;[2] in the meantime, the calculations were implemented with polarizable continuum model (PCM) for all systems. All the calculations were carried out by using the Gaussian 16 (revision A03) program. The adsorption models were analyzed by Multiwfn (revision 3.8),[3] and the images of structures were obtained from Visual Molecular Dynamics (VMD, revision 1.9.3). As a result, the adsorption energies were calculated by as-described methods and illustrated in this work with an ascending order (-0.79 eV ($H_2O(HPO_3)_1$@CN), -0.88 eV ($H_2O(HPO_3)_2$@CN), and -1.30 eV ($H_2O(HPO_3)_3$@CN).

For the ionic liquid $CF_3SO_3^-$, the anion system has a significant negative charge, and its electrons are easily polarized. The calculation method was slightly adjusted, and the diffuse function M06-2X/6-31+G(d,p) was used for the calculation, the adsorption energy is -0.46 eV ($CF_3SO_3^-$@CN). Owing to the difference in the calculation methods, this result can only be qualitatively compared with the adsorption energy of phosphoric acid.

Results and Discussion
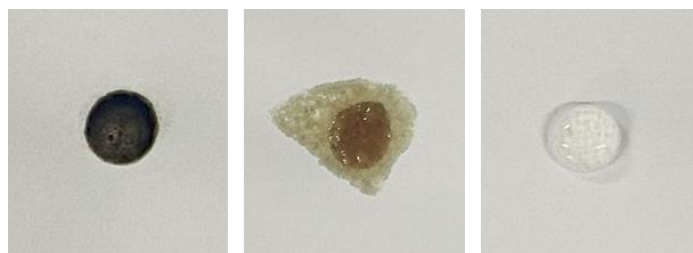
Figure S1. Photographs of a drop of concentrated sulfuric acid, methyl sulfonic acid and PPA (from left to right) dropped on the paper after a few seconds.

In order to evaluate the structure damage to carbonaceous materials by acids, a drop of concentrated sulfuric acid, methyl sulfonic acid and PPA were dropped on the paper simultaneously. It was found that concentrated sulfuric acid and methyl sulfonic acid carbonized paper severely; in contrast, PPA was much milder.
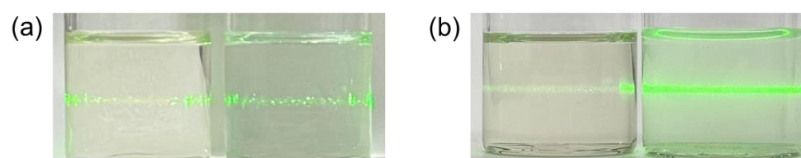
Figure S2. (a) Tyndall phenomenon of pCN-PPA solution and pure solvent. (b) Tyndall phenomenon of pCN dissolved in PPA and dispersed in H_2O.

PPA is formed by the dehydration and condensation between multiple PA molecules. The content of phosphorus pentoxide (P_2O_5) could be adjusted easily by regulating the proportion of PPA and PA to control the amount of free hydrogen ions and viscosity of acid. As the molecular weight of PPA increases, the solvent will be sticky and change from liquid to solid at room temperature.

Tyndall phenomenon was used to determine whether pCN-PPA solution formed. Experimentally, the Tyndall phenomenon of the original PPA solvent was also observed, which kept the same after the dissolution of pCN (Figure S2a). In contrast, when pCN was dispersed in water, the Tyndall phenomenon increased obviously (Figure S2b).

Figure S3. Photographs of pCN dissolved in PPA at different concentrations (2 mg/mL, 10 mg/mL, 50 mg/mL, from left to right).
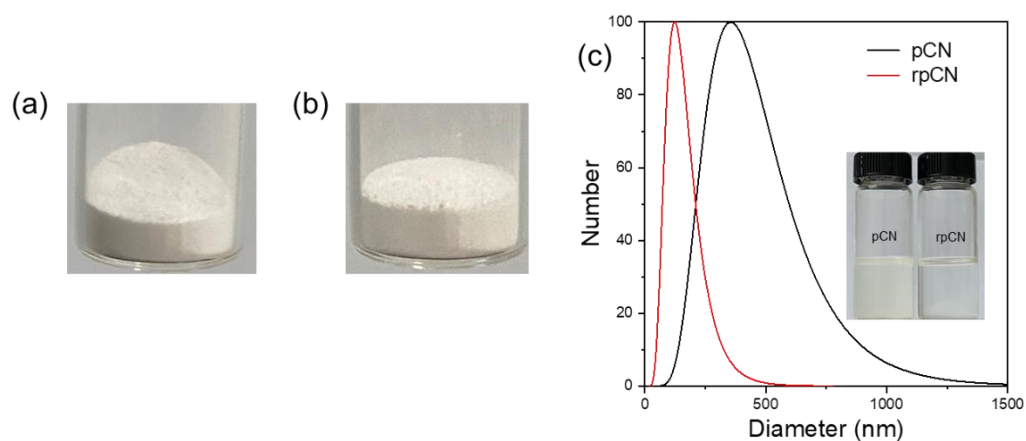
Figure S4. Photographs of (a) melem and (b) melam. (c) DLS size distribution of pCN and rpCN. Insets: photographs of pCN and rpCN dispersion in water.

Oligomers of carbon nitrides like melem or melam are usually white.

Considering the particle size distribution and the clearer dispersion in water, the size of rpCN was smaller than pCN.
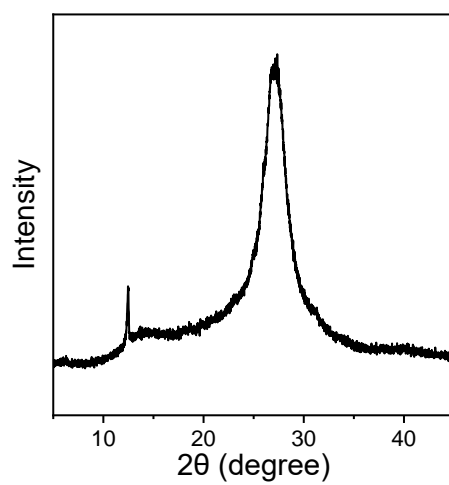
Figure S5. XRD pattern of rpCN powder after calcination at 250 °C for 10 h.

Diffraction peaks marked with asterisks in Figure 1c were from impurities, as they disappeared after calcined at 250 °C in tubular furnace.
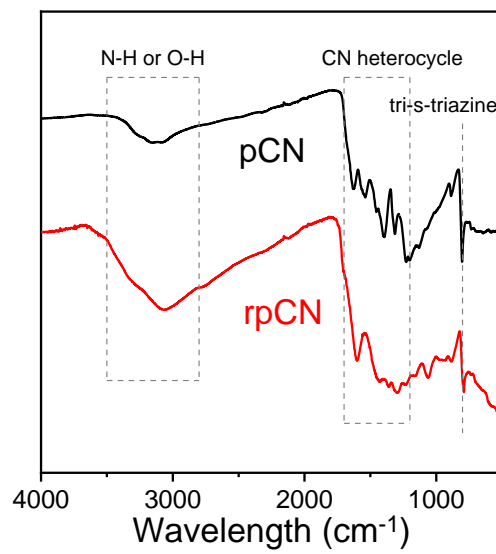
Figure S6. FT-IR spectra of pCN and rpCN.
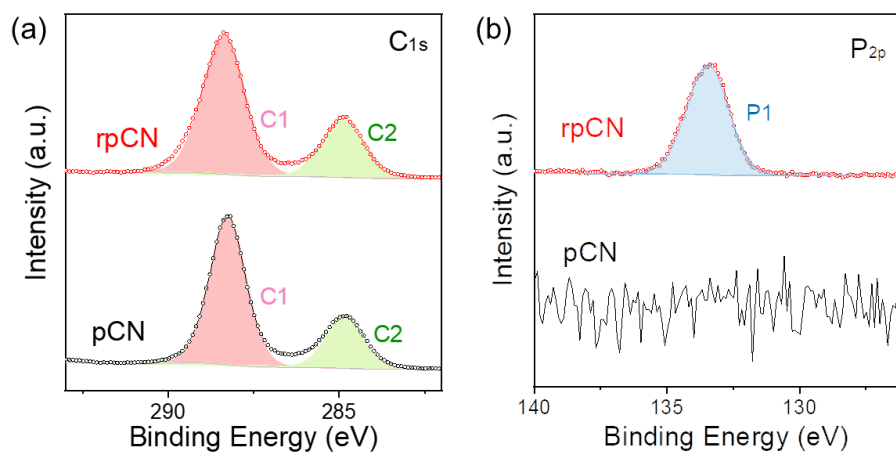
Figure S7. XPS C_{1s} (a) and P_{2p} (b) spectra of pCN and rpCN.

In XPS P_{2p} spectra, the peak of P appeared in rpCN, demonstrating the presence of phosphoric acid compared with pristine pCN. A new P_{2p} component at 133.4 eV was within the energy characteristic range of PO_4^{2-}, showing the effective protonation of pCN in PPA.
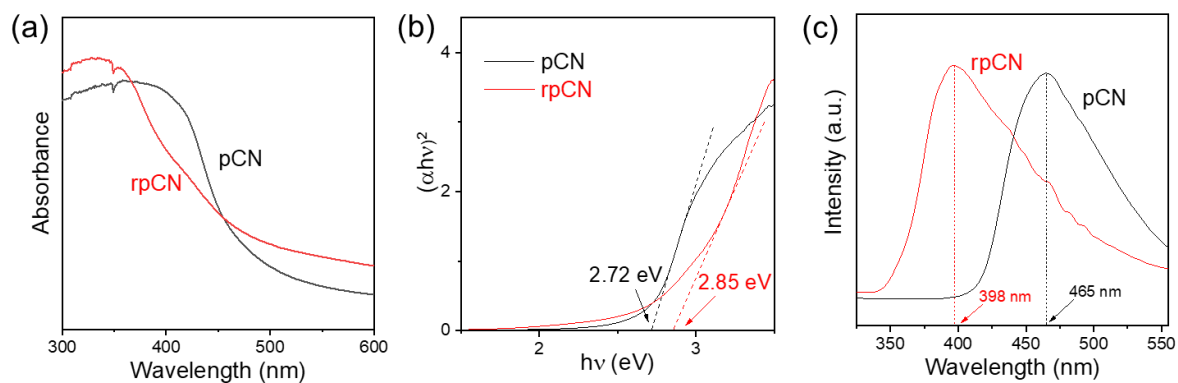
Figure S8. UV-Vis absorption (a) and corresponding Tauc plot (b) of pCN and rpCN. (c) FL spectra of pCN and rpCN.

Figure S9. Photograph of pCN-PPA paste (600 mg/mL) on a glass.
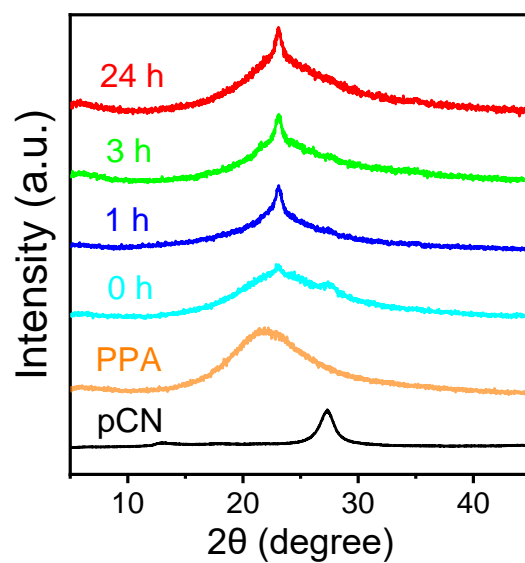
Figure S10. XRD patterns of PPA, pCN and the mixture of pCN and PPA paste (600 mg/mL, 75% P_2O_5) with different treat time.
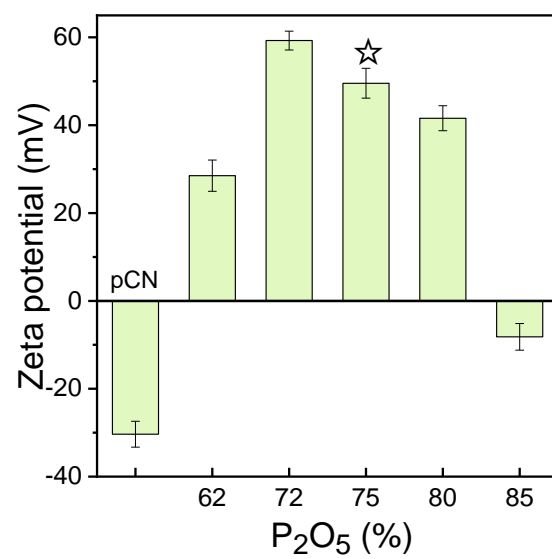
Figure S11. Zeta potential of pCN and rpCN precipitated from PPA with different P_2O_5 contents.
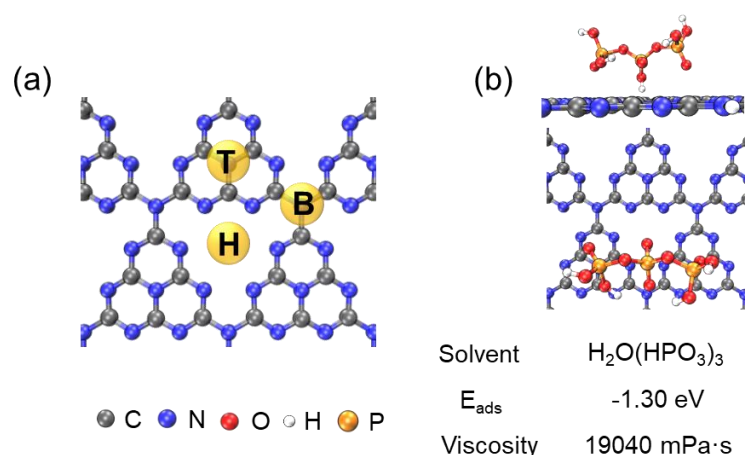
Figure S12. (a) Typical adsorption sites on carbon nitride monolayer structure: top (T), hollow (H), bridge (B). (b) The most stable adsorption structure of P3 molecule on pCN.

The adsorption sites of top (T), bridge (B) and hollow (H) are optimized firstly. The hollow (H) position is the most stable adsorption site, performing calculations around H structure. According to the literature,[2] the adsorption energy of concentrated sulfuric acid and methyl sulfonic acid reported previously were -0.73 eV and -0.84 eV, respectively. The result in this paper was similar to them. However, tri-polyphosphoric acid (P3) with a higher E_{ads} and viscosity exhibited a negligible solubility. This may beyond the scope of wet chemistry that the phase change of solvent need to be taken into account in future research.
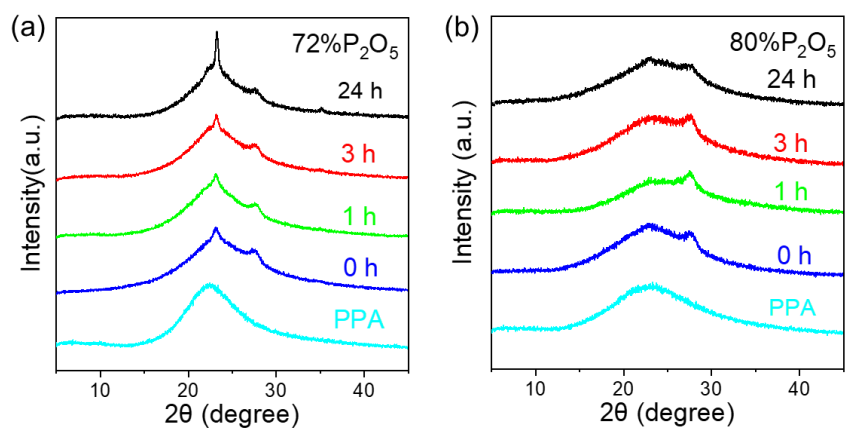
Figure S13. XRD patterns of pCN-PPA paste at different treat time. (a) 72% P_2O_5; (b) 80% P_2O_5.
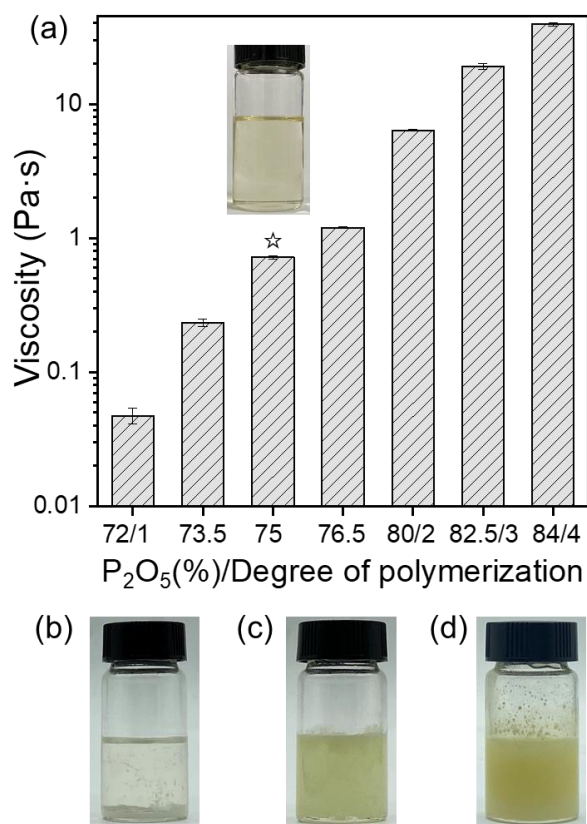
Figure S14. (a) Viscosity of PPA with different P_2O_5 content. The numbers 1 to 4 on the abscissa represent the monomer number of the corresponding polyacid. Inset: photograph of pCN dissolved in PPA (75% P_2O_5). Photographs of pCN dispersed in (b) P1, (c) P2 and (d) P3.
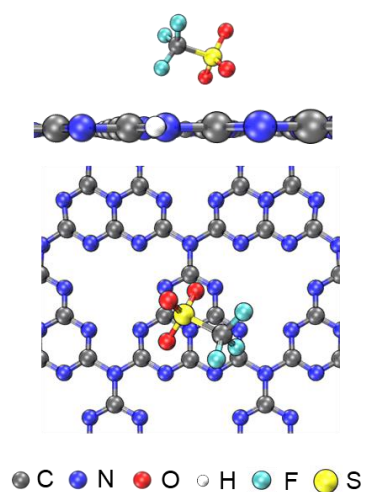
Figure S15. The most stable adsorption structure of $CF_3SO_3^-$ on pCN.

The E_{ads} of BSO_3Py^+-$CF_3SO_3^-$ was calculated to be -0.46 eV. The viscosity of BSO_3Py^+-$CF_3SO_3^-$ is 536 mPa·s.
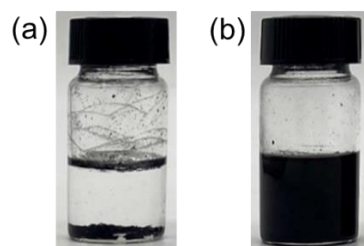
Figure S16. Photographs of carbon nanotubes dispersed in H_2O (a) or PPA (b).
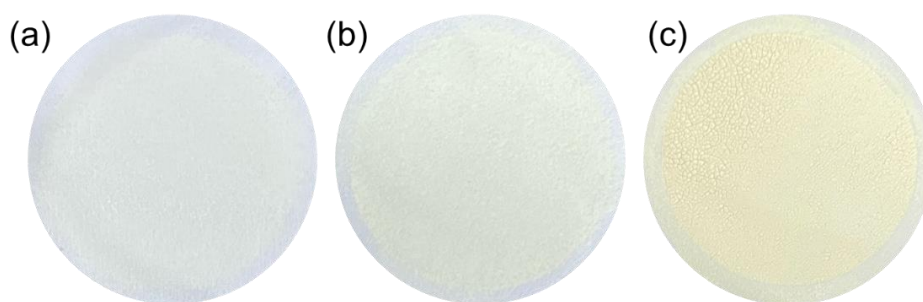
Figure S17. Photographs of carbon nitride nanosheets (CNNS) with different concentrations and volumes after filtering. (a) 0.02 mg/mL, 200 mL; (b) 0.02 mg/mL, 500 mL; (c) 0.1 mg/mL, 500 mL. The white filter membrane was PTFE.

Bulk carbon nitride was too rigid to form a membrane. At a low concentration,[4] a few amounts of CNNS dispersion appeared to form a membrane, but the film was too thin and could not be peeled from the filter membrane. When the concentration and the volume of CNNS dispersion increased, the film started to crack when dried.
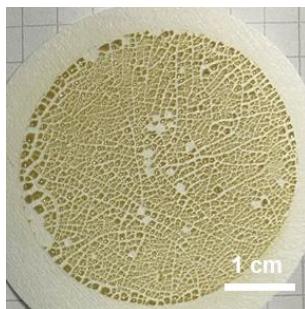
Figure S18. Photograph of rpCN. The white filter membrane was PTFE.
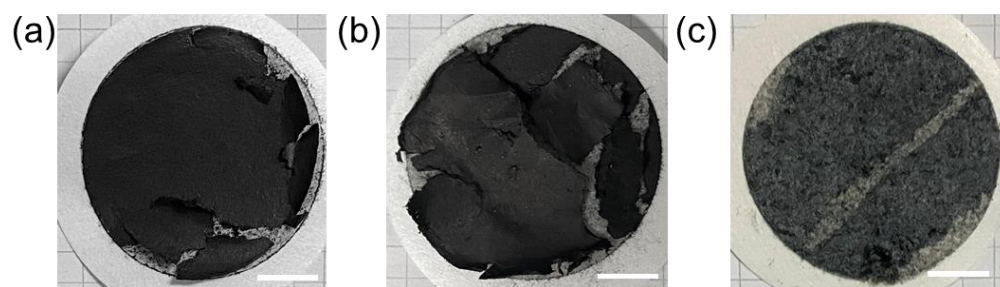
Figure S19. Photographs of (a) CNTs membrane and (b) pCN+CNTs membrane by filtration, and (c) CNNS+CNTs dispersed in water by filtration. The white filter membrane was PTFE. Scale bars: 1 cm.
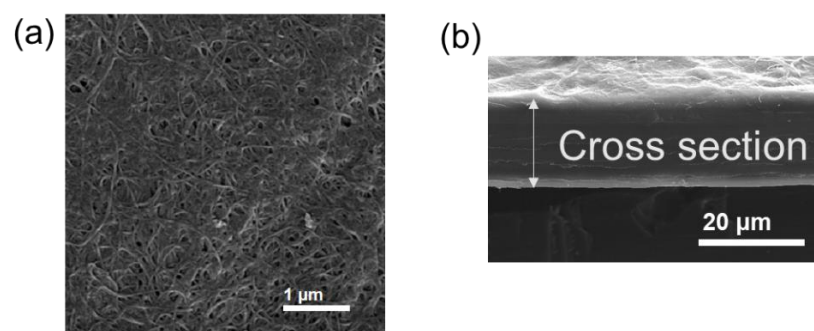
Figure S20. (a) Top surface SEM image of pCN/CNTs membrane. (b) Cross-sectional SEM image of pCN/CNTs membrane.
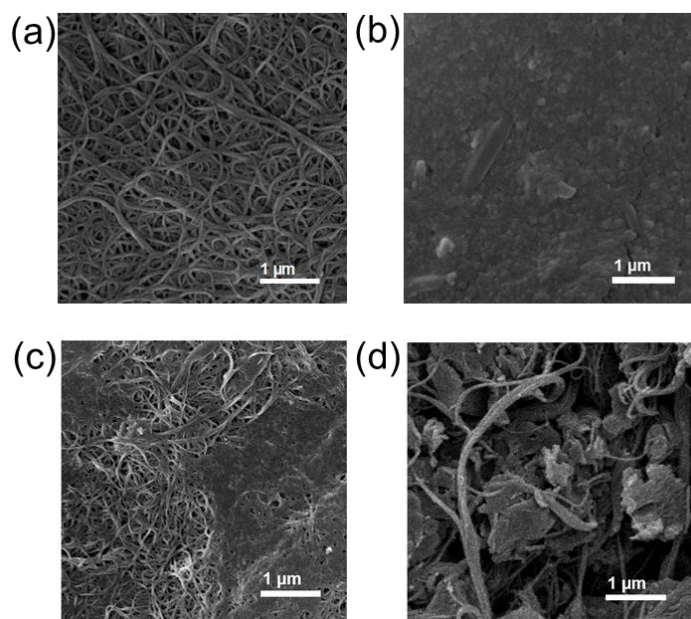
Figure S21. SEM images of (a) CNTs membrane, (b) rpCN, (c) pCN+CNTs membrane, and (d) CNNS+CNTs dispersed in water.

Compared to the pCN/CNTs membrane, the pCN+CNTs membrane had an unevenly distributed pCN and CNTs, owing to the lacking of PPA compounding. In contrast, without PPA, the dispersion of pCN and CNTs in water was poor, and it was impossible to get a membrane at all. From the SEM image of CNNS+CNTs in water, it could be seen that CNNS and CNTs existed separately and there were large gaps between them.
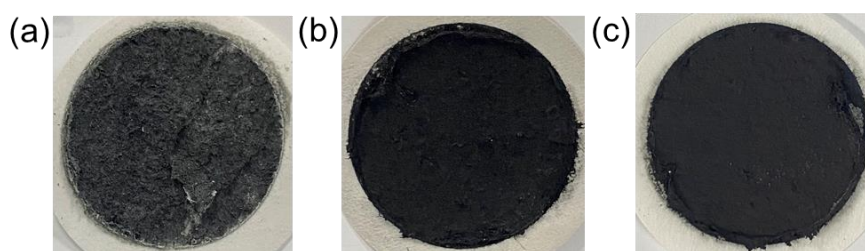
Figure S22. Photographs of pCN and CNTs dispersed in hydrochloric acid (a), concentrated sulfuric acid (b) and methyl sulfonic acid (c) by filtration. The white filter membrane was PTFE.

Replacing PPA with hydrochloric acid (HCl), concentrated sulfuric acid (H_2SO_4) or methyl sulfonic acid (MSA), none of them could form membranes as good as that by PPA. The mixture using hydrochloric acid showed obvious phase separation; concentrated sulfuric acid and methyl sulfonic acid had better solubility than hydrochloric acid, but they exhibited many flocculent CNTs and partially exposed pCN, rather than a complete membrane after filtration.
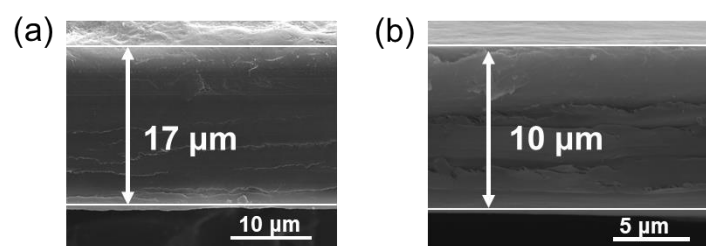
Figure S23. Cross-sectional SEM images of the pCN/CNTs membrane with different starting materials.

The thickness of the pCN/CNTs membrane could be easily regulated by changing the amount of the starting material. At the same concentration, the starting material volume ratio of Figure S23a and S23b was about 2:1
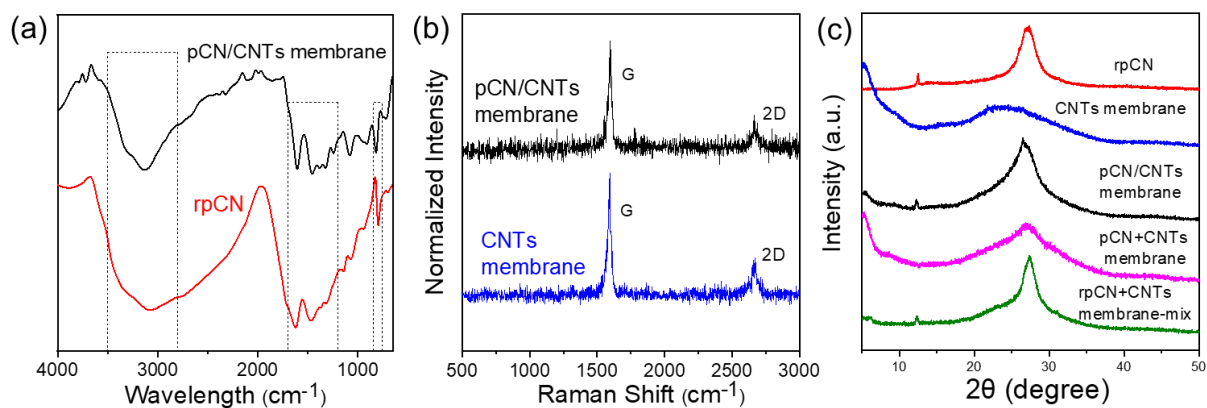
Figure S24. (a) FT-IR spectra of rpCN and the pCN/CNTs membrane. (b) Raman spectra of the CNTs membrane and pCN/CNTs membrane. (c) XRD patterns of rpCN, the CNTs membrane, the pCN/CNTs membrane, the pCN+CNTs membrane, and the mixture of rpCN and CNTs membrane (grind).
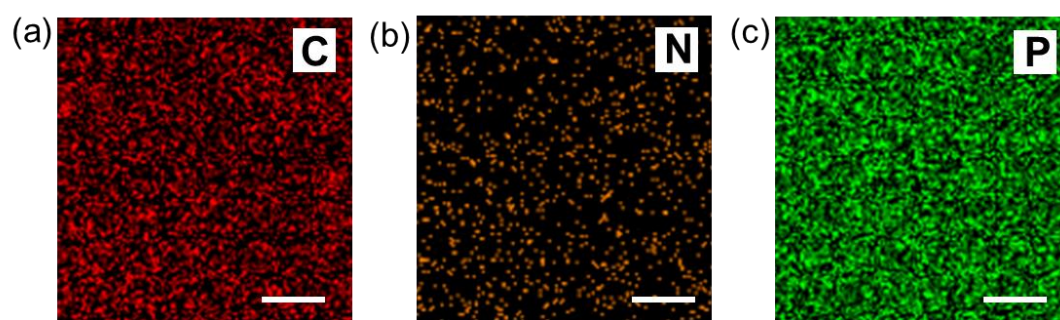
Figure S25. Top surface EDS elemental mappings of pCN/CNTs membrane. Scale bars: 1 μm.
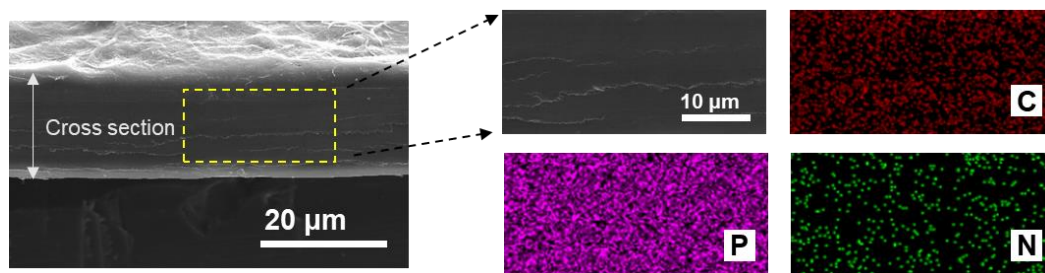
Figure S26. Cross-sectional SEM image of the pCN/CNTs membrane and the EDS elemental mappings.
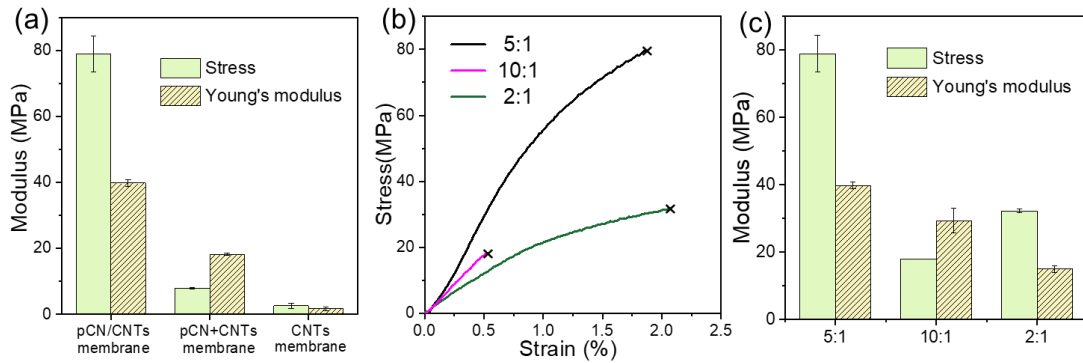
Figure S27. (a) Ultimate strength and Young's modulus of pCN/CNTs membrane, pCN+CNTs membrane and CNTs membrane. (b) Stress-strain curves of pCN/CNTs membrane with different pCN:CNTs weight ratios. (c) Ultimate strength and Young's modulus of pCN/CNTs membrane with different pCN:CNTs weight ratios.

With the increase of pCN content, ultimate strength and Young's modulus of the membrane decreased to some extent. Probably, the excessive pCN made the membrane more brittle and less compact. The ratio of pCN to CNTs (5:1) was regarded as the optimum one in this work. Notably, the yield of pCN by precipitation was about 15%-20%, and the yield of CNTs by precipitation was 85%-90%. The final amount of carbon nitride on the membrane was about 50%.
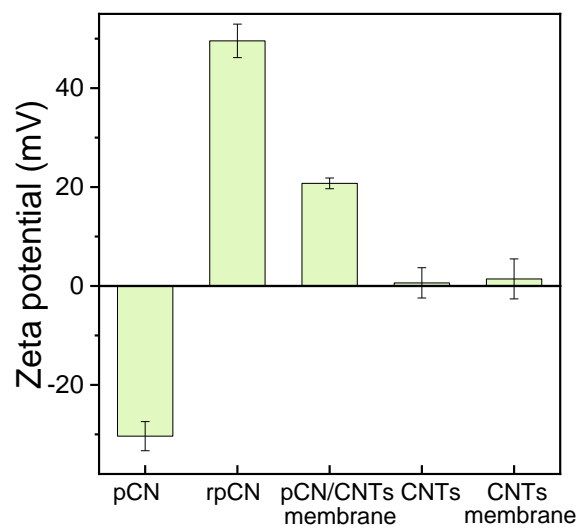
Figure S28. Zeta potential of pCN, rpCN, pCN/CNTs membrane, CNTs, and CNTs membrane after dispersion in water.
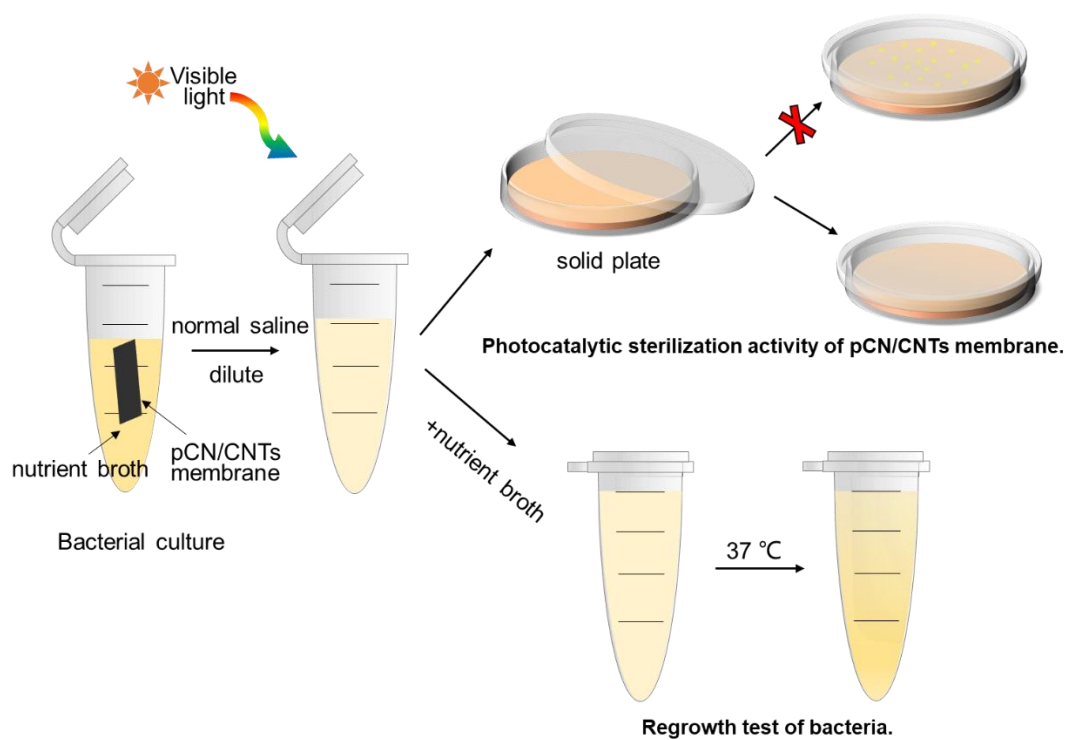
Figure S29. The experimental processes of photocatalytic sterilization activity of pCN/CNTs membrane and regrowth test of bacteria.
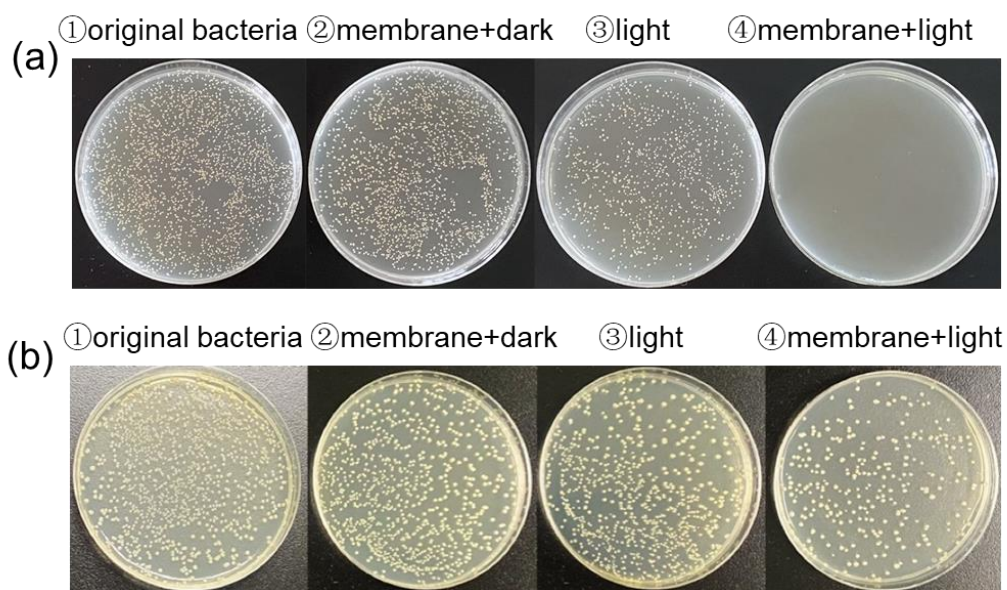
Figure S30. Photographs of bacterial colonies of (a) *S. aureus* and (b) *E. coli.* From left to right: original bacteria, bacteria with pCN/CNTs membrane in dark, bacteria without pCN/CNTs membrane under visible light, bacteria with pCN/CNTs membrane under visible light.

Since the pCN/CNTs membrane and rpCN were positively charged and bacteria were negatively charged,[5] the electrostatic attraction of the membrane acted a positive role in the sterilization process. Gram-positive bacteria had a lower isoelectric point and carried more negative charge, so the sterilization effect of *S. aureus* was better.

Note: In this paper, the concentration of bacteria was not completely quantified in all experiments, but maintained the same concentration in the same comparison experiments. Because of the lighting, the color of colonies may look like a little different to the conventional ones.
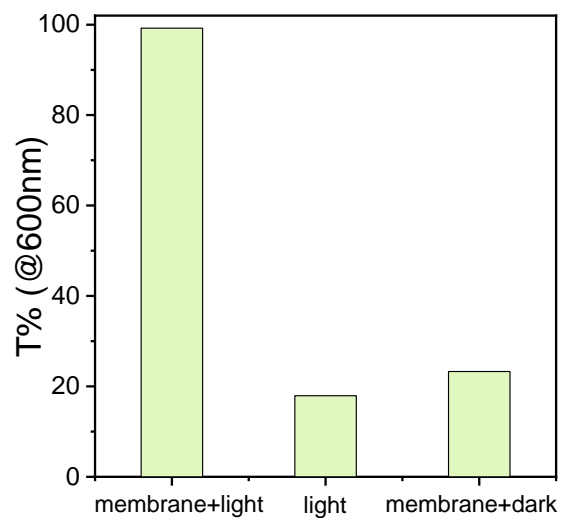
Figure S31. The transmittance at 600 nm for *S. aureus* in different conditions (bacteria with pCN/CNTs membrane under visible light, bacteria without pCN/CNTs membrane under visible light, and bacteria with pCN/CNTs membrane in dark).[5]
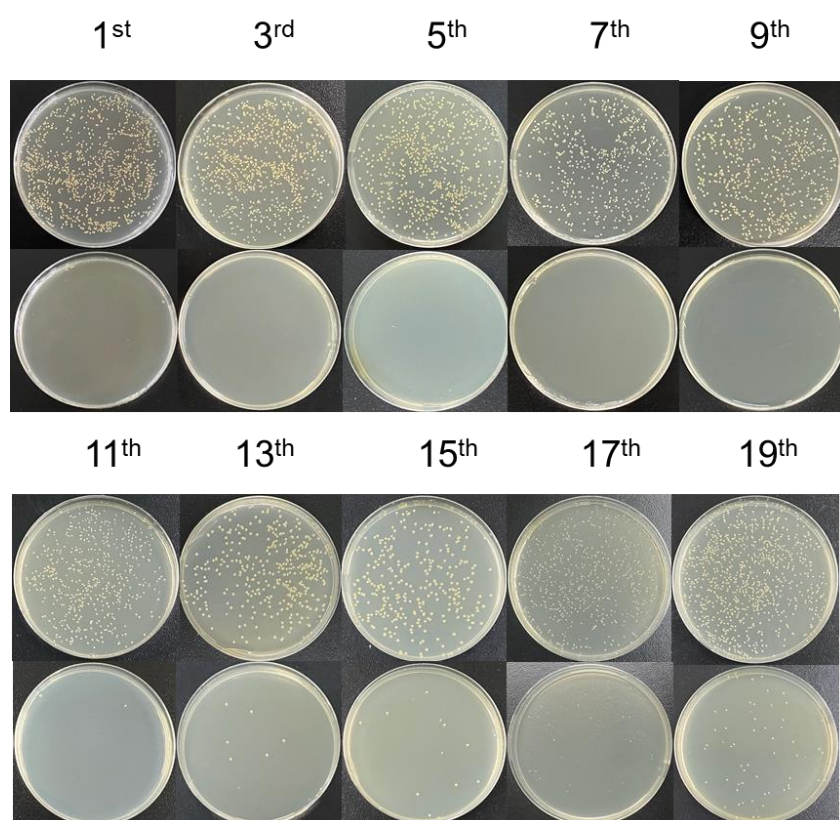
Figure S32. Photographs of bacterial colonies of *S. aureus* after incubating with pCN/CNTs membrane under visible light 1 h for twenty cycles.
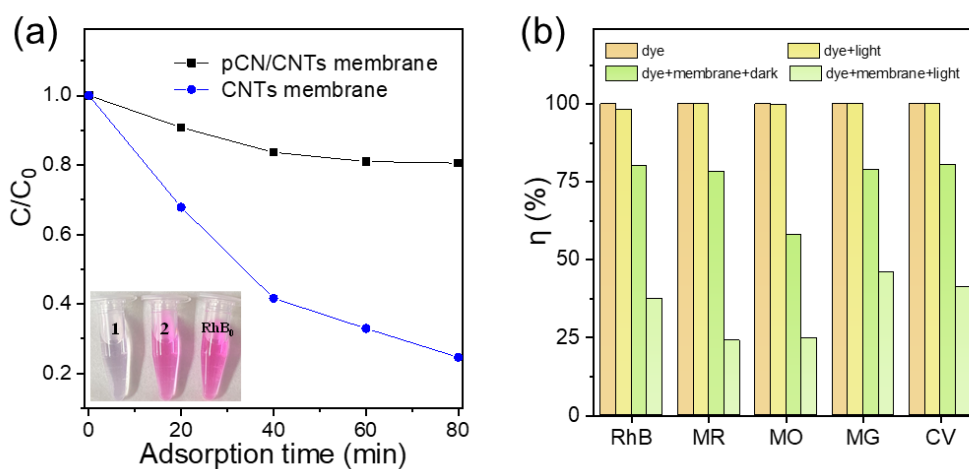
Figure S33. (a) The adsorption capacity of pCN/CNTs membrane and CNTs membrane. Insets: the color comparison of RhB after physical adsorption in dark: **1** corresponds to CNTs membrane, **2** corresponds to pCN/CNTs membrane. (b) Absorbance changes of different dyes including RhB, Methyl Red (MR), Methyl Orange (MO), Methyl Green (MR), and Crystal Violet (CV) with or without pCN/CNTs membrane and with or without illumination.

The physical adsorption capacity of CNTs membrane was very strong due to the large specific surface area. When introduced pCN to prepare pCN/CNTs membrane, the adsorption reduced. The pCN/CNTs membrane had a certain degree of adsorption for a variety of dyes in dark. When illuminated under visible light, the degradation effect of dyes was obviously enhanced. From Figure S33b, it can be seen that the dye degradation was mainly resulted from the photocatalytic effect rather than the physical adsorption effect.
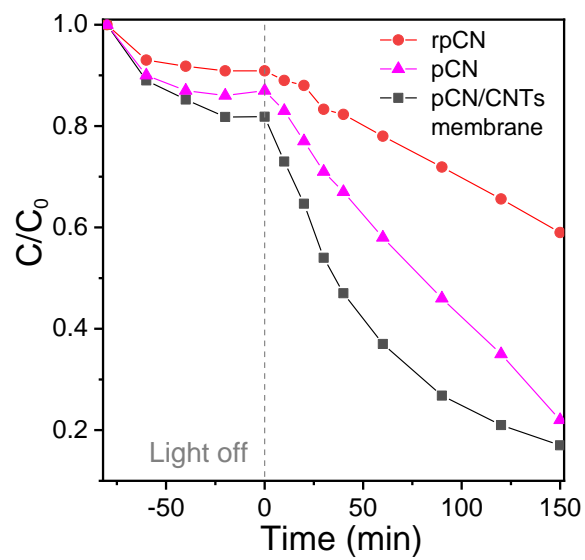
Figure S34. Absorbance of RhB at 554 nm as a function of time during photocatalysis (> 400 nm) using pCN, rpCN and pCN/CNTs membrane.
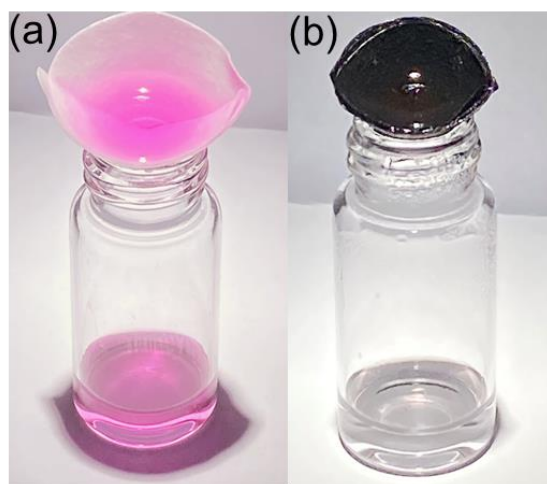
Figure S35. Photographs of filtration of RhB dye using ordinary filter paper (a) and pCN/CNTs membrane (b) under the light irradiation.

Figure S35 showed the RhB dye solution filtered through pCN/CNTs membrane under visible light. Under the light irradiation, the filtered water through the pCN/CNTs membrane became colorless. In contrast, the dye solution passed through ordinary filter papers was unchanged.
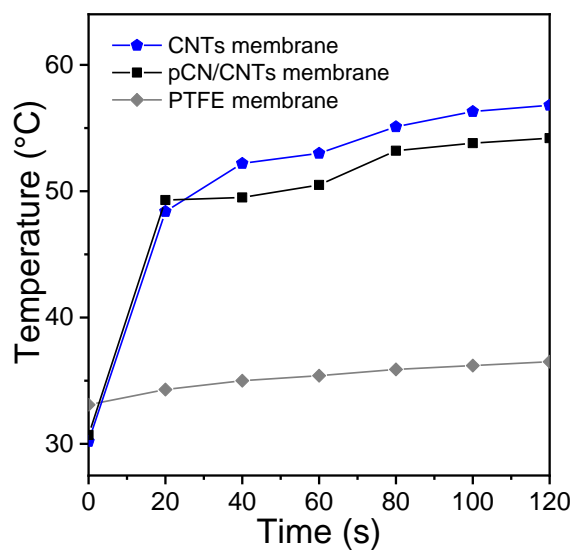
Figure S36. Surface temperature enhancement of CNTs membrane, pCN/CNTs membrane and PTFE membrane under Xe light irradiation.

As the pCN/CNTs membrane was black, the photothermal effect was taken into account.[6] The surface temperature of different membranes under simulated sunlight were examined by using a noncontact infrared thermometer. The surface temperature of the blank white PTFE membrane almost stayed unchanged in two minutes, while the temperature of CNTs membrane and pCN/CNTs membrane increased for ca. 20 °C.
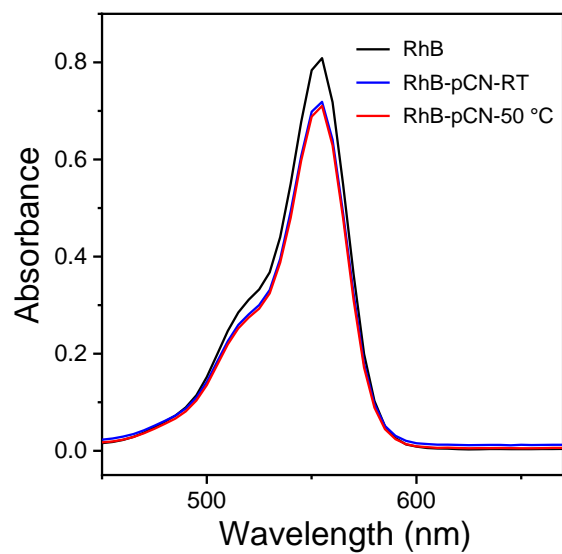
Figure S37. UV-Vis absorption of RhB solution, RhB with pCN at room temperature and 50 $^{\circ}$C.

After increasing the temperature from room temperature to 50 $^{\circ}$C, the absorbance of RhB-pCN did not decrease significantly, indicating that pCN did not have thermal effect to generate ROS.
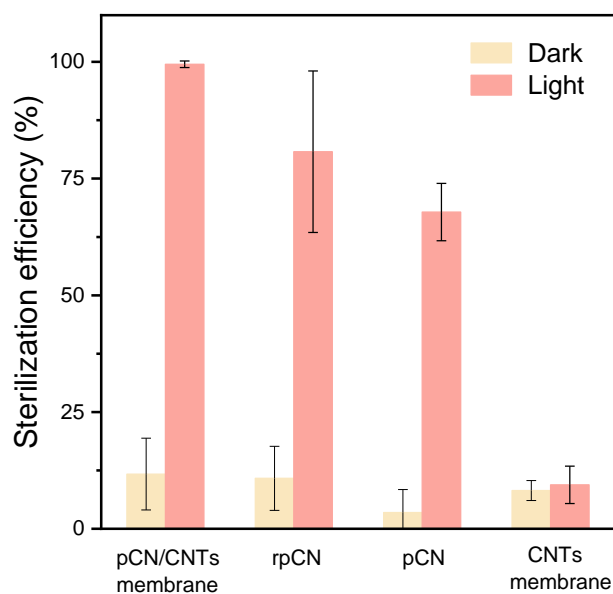
Figure S38. Comparison of the sterilization efficiency for *S. aureus* between pCN/CNTs membrane, rpCN, pCN and CNTs membrane under light and dark conditions, respectively.

The sterilization efficiency of CNTs membrane was very poor, manifesting that photothermal effect is not the main factor. The performance of pCN was poorer than rpCN, because of the helpful electrostatic attraction between membrane and bacteria. As the negatively charged bacteria cells had poor contact with pCN that is also negatively charged.
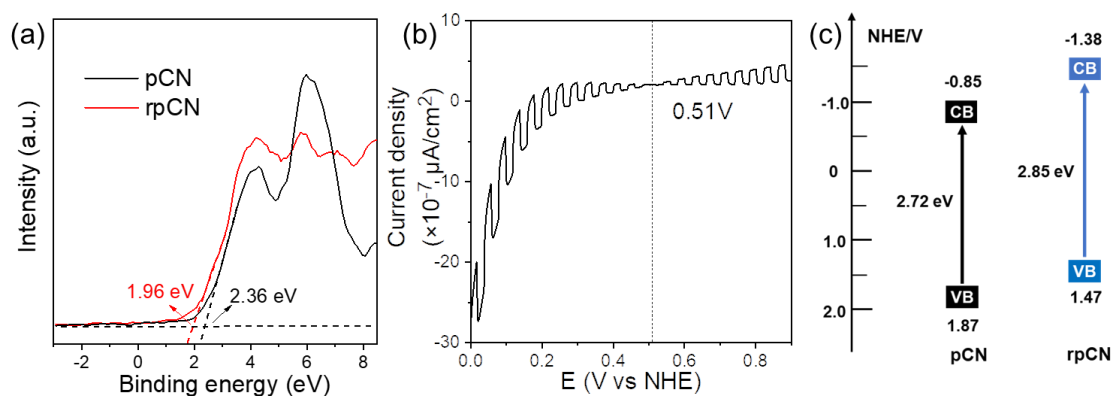
Figure S39. (a) XPS-VB of pCN and rpCN. (b) Chopped current-potential (I-V) curve and Fermi level of pCN photoelectrode under visible light.[7] (c) The calculated energy band structure of pCN and rpCN.

The photoelectrochemical measurements were performed in a traditional three-electrode system in a quartz tank with a platinum wire as the counter electrode and Ag/AgCl (saturated KCl) electrode as the reference electrode. The potentials were measured against the Ag/AgCl electrode (saturated KCl) and converted to versus Normal Hydrogen Electrode (NHE) according to the Nernst equation ($E_{NHE} = E_{Ag/AgCl} + 0.199$).

Combining the results of UV-vis, XPS-VB spectra and the position of Fermi level, the band structure of rpCN could be obtained.[7, 8]
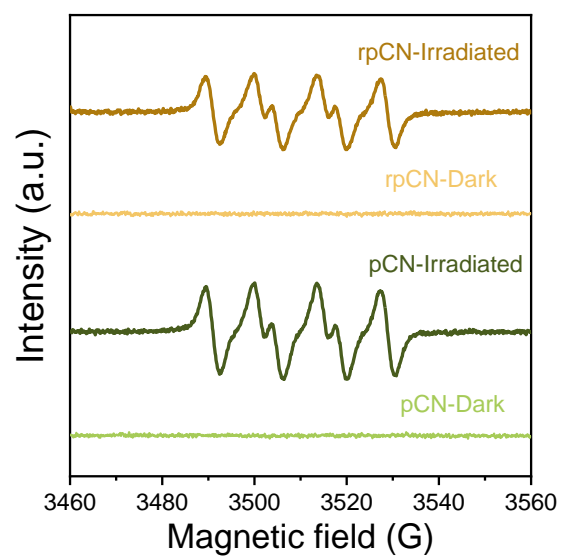
Figure S40. EPR spectra of DMPO-•O_2^- for rpCN and pCN under light irradiation and in dark.
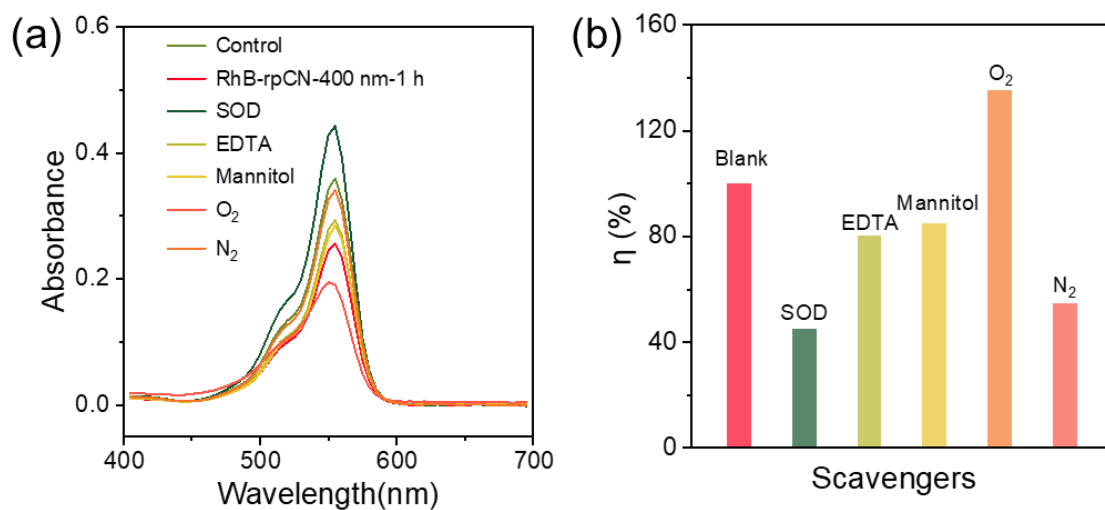
Figure S41. UV-Vis absorption (a) and photocatalytic activity (b) of rpCN for RhB degradation in the presence of different scavengers under 400 nm light source.

The trapping experiments of rpCN, which was used to represent the carbon nitride on the pCN/CNTs membrane, were conducted to explore the possible intermediate reactive species.[9,10] It was observed that the RhB dye degradation efficiency of rpCN appeared a various degree of inhibition by adding $\cdot O_2^-$, hole or $\cdot OH$ scavengers.[11] It was restrained distinctly when SOD was added into the reaction solution. When O_2 was introduced into the solution, the efficiency was drastically improved; while it presented an opposite result when Ar was purged into the solution, revealing that O_2 was a vital co-substrate, and the activation of O_2 by reduction via photogenerated electrons into $\cdot O_2^-$ was the major step for bactericidal and small molecule conversion.
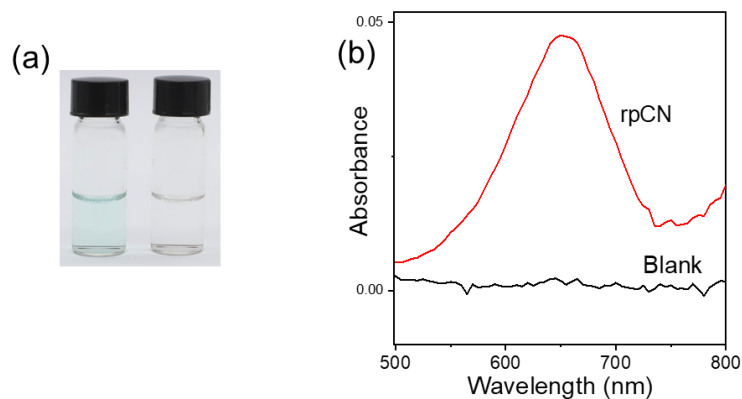
Figure S42. Photographs (a) and UV-Vis absorption (b) of TMB aqueous solution with (left, red) and without (right, black) rpCN under visible light.

In order to check whether H_2O_2 was generated or not, rpCN dispersion was irradiated for 1 h. Horseradish peroxidase (HRP) and 3,3′,5,5′-Tetramethylbenzidine (TMB) were then added and incubated for 5 mins after the removal of rpCN by centrifugation. Colorless TMB would be catalyzed by HRP into blue TMB_{ox}[12] if H_2O_2 was presented. The solution changed from colorless to blue with the addition of rpCN, and the typical absorbance of TMB_{ox} appeared, thus proving H_2O_2 was produced. We speculated that a few $\bullet O_2^-$ was converted to H_2O_2 and then turned into $\bullet OH$ acted together with $\bullet O_2^-$.
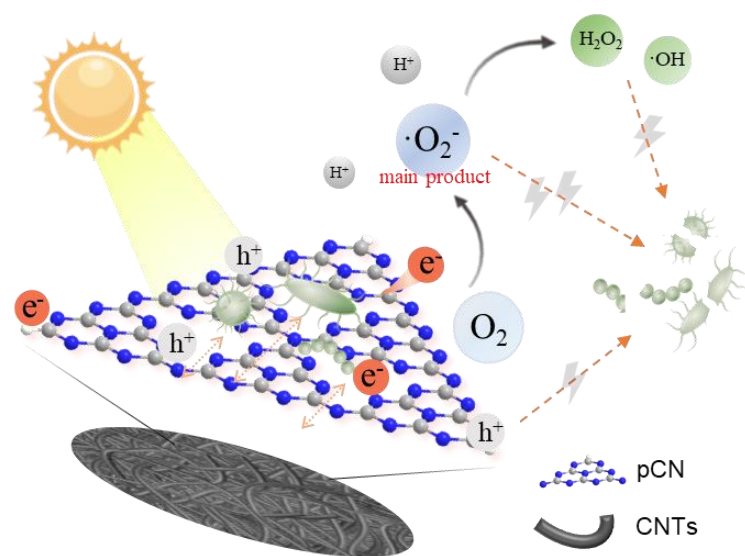
Figure S43. Photocatalytic sterilization mechanism of the pCN/CNTs membrane.
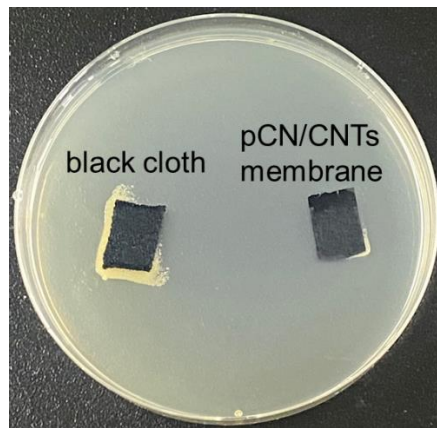
Figure S44. Antibacterial effect comparison of control black cloth and pCN/CNTs membrane.
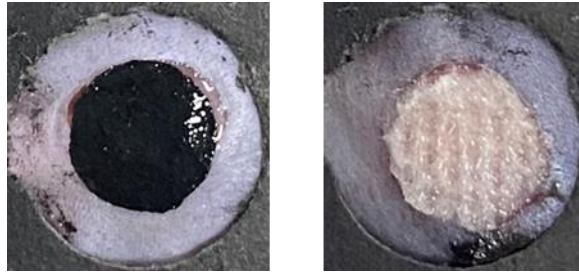
Figure S45. Photograph of the *S. aureus*-infected wound of mice covered with pCN/CNTs membrane (left) and the control general gauze (right).
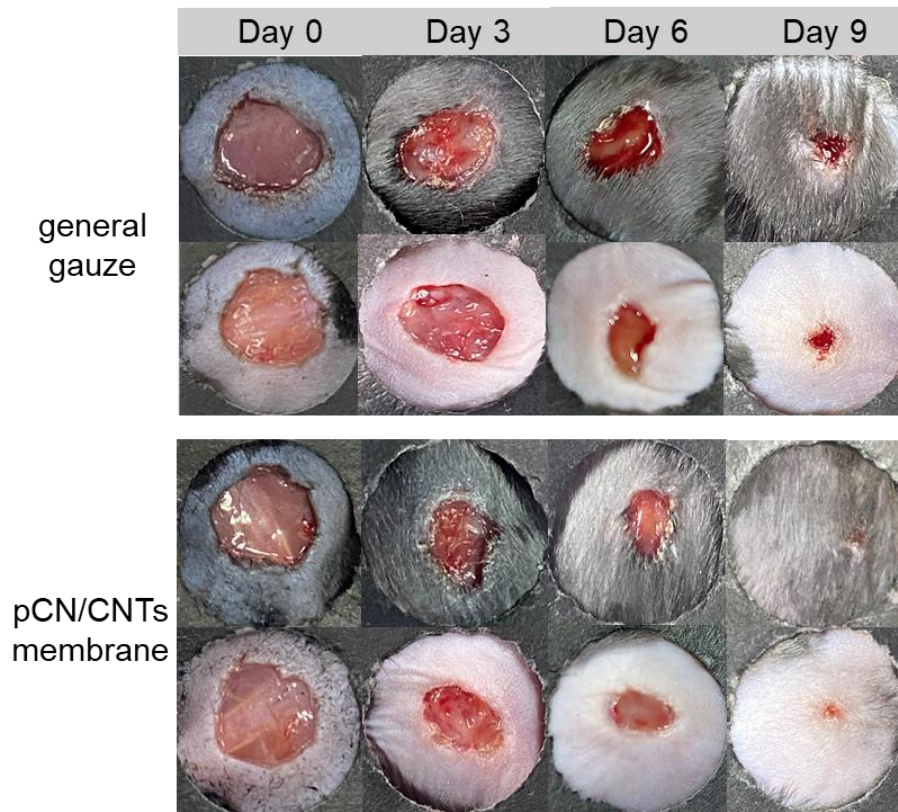
Figure S46. Photographs of the *S. aureus*-infected wounds in two of the five groups of mice treated with pCN/CNTs membrane and general gauze for different times.
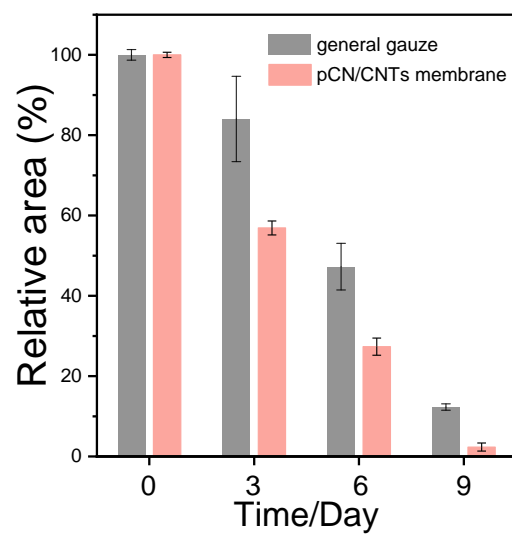
Figure S47. The closure rate of the wounds on the mice treated with pCN/CNTs membrane and general gauze for different time.
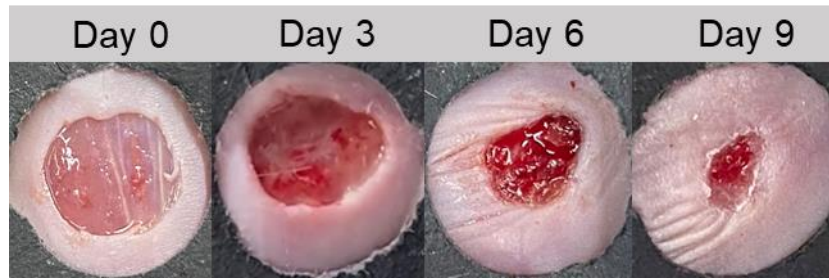
Figure S48. Photographs of *S. aureus*-infected wounds in laboratory mice under sunlight without pCN/CNTs and general gauze at different time.

Table S1. pK$_a$ values of different acids measured by MarvinSketch.

	pK$_{a1}$	pK$_{a2}$	pK$_{a3}$	pK$_{a4}$
HCl	-7	-	-	-
H$_2$SO$_4$	-3.03	1.90	-	-
MSA	-1.61	-	-	-
HNO$_3$	-1.40	-	-	-
H$_4$P$_2$O$_7$	0.04	0.85	5.31	6.08
H$_3$PO$_4$	1.80	6.95	12.90	-

The software MarvinSketch (https://chemaxon.com/marvin) was used to simulate molecular structures of different acids and calculate their pK$_a$ values to compare acidity levels.

Table S2. Elemental analysis of pCN and rpCN.

	Element	(wt. %)	Atom (%)	Molar ratio
	C	34.24	30.19	
pCN	N	60.30	45.66	C/N = 0.66
	H	2.07	21.93	
	O	3.39	2.22	
	C	23.77	18.98	
rpCN	N	44.98	30.78	C/N = 0.62
	H	3.67	35.19	
	O	22.58	13.52	

*Due to the presence of P, the sum of C/N/H/O in rpCN was not 100%.

The C/N molar ratios of pCN and rpCN were approximately equal, and it decreased slightly due to the carbon loss and defect reduction during the process of dissolution and precipitation.

Table S3. Bacteria disinfection by CN-based and other traditional photocatalysts.

Photocatalysts	State	Property	Light (λ)	Bacteria	Dosage g/L	Performance $\log_{10}(C_0/C)$ Efficiency	Ref.
pCN/CNTs	Membrane	Metal-free	> 400 nm	*S. aureus* *E. coli*	0.3	6	This work
g-C$_3$N$_4$	Powder	Metal-free	> 420 nm	*E. coli K-12*	1	6	[13]
CN-S	Powder	Metal-free	> 420 nm	*E. coli K-12*	1	8	[14]
BT-CN	Powder	Metal-free	> 420 nm	*E. coli*	5	7	[15]
SL g-C$_3$N$_4$	Powder	Metal-free	> 400 nm	*E. coli*	0.1	7	[16]
AHUCN	Powder	Metal-free	> 400 nm	*E. coli*	1	7.48	[17]
g-C$_3$N$_4$/P	Powder	Metal-free	> 420 nm	*E. coli*	1	7	[18]
CNTs-PAA/CNMS	Powder	Metal-free	> 420 nm	*E. coli* *S. aureus* *P. mirabilis*	N/A	4	[19]
TPCN	Powder	Metal-free	> 420 nm	*E. coli*	0.4	6.67	[20]
ACHT-g-C$_3$N$_4$ nanosheets	Powder	Metal-free	> 420 nm	*E. coli*	1	7.39	[21]
F-g-C$_3$N$_4$-30-EP	Film/glass	Metal-free	> 400 nm	*E. coli K-12* *Salmonella*	0.01	6	[22]
Bulk g-C$_3$N$_4$	Powder	Metal-free	> 400 nm	*MS2*	0.15	8	[23]
TRP	Powder	Metal-free	> 400 nm	*E. coli K-12*	0.5	7	[24]
g-C$_{3.6}$N$_4$/PVA	Hydrogel	Metal-free	> 420 nm	*E. coli*	N/A	6	[25]
Ag/g-C$_3$N$_4$	Powder	Metallic	> 400 nm	*E. coli K-12*	0.1	4.67-7.41	[26]
Ni$_2$P/g-C$_3$N$_4$	Powder	Metallic	> 420 nm	*E. coli*	N/A	7	[27]
g-C$_3$N$_4$-AuNPs	Powder	Metallic	670nm	*E. coli*	0.2	N/A	[28]
g-C$_3$N$_4$/TiO$_2$/ kaolinite	Powder	Metallic	> 400 nm	*S. aureus*	0.03	3	[29]
PCNS	Powder	Metal-free	> 420 nm	*E. coli*	0.4	6.7	[30]
GO-CdS	Powder	Metallic	≥ 420 nm	*E. coli*	0.1	7	[31]
CoFe$_2$O$_4$/HTCC	Powder	Metallic	> 400 nm	*E. coli K-12*	1	7	[32]
TiO$_2$NT/CdS	Film/Glass	Metallic	No data	*E. coli* *XL1 Blue*	N/A	2	[33]

BV-NT	Powder	Metallic	> 400nm	*E. coli K-12*	0.1	5.3	[34]
Ag_3PO_4-rGO	Coated textiles	Metallic	No data	*S. aureus* *E. coli*	N/A	N/A	[35]
rGO-AgNP/$Bi_2Fe_4O_9$	Powder	Metallic	420-630 nm	*E. coli*	0.1	6	[36]
COF-TfpBpy	Powder	Metallic	> 420nm / > 300nm	*E. coli*	N/A	5	[37]

Table S4. Properties of the CNTs used this work provided by the manufacturer.

Property	Unit	Numerical value
Outer Diameter	nm	< 2
Purity	wt%	> 95
Length	Microns	5-30
Specific Surface Area	m^2/g	> 900
ASH	wt%	< 2.5
Ignition Point	℃	697

Supporting references

1. Z. Zhou, J. Wang, J. Yu, Y. Shen, Y. Li, A. Liu, S. Liu and Y. Zhang, Dissolution and liquid crystals phase of 2D polymeric carbon nitride, *J. Am. Chem. Soc.*, 2015, **137**, 2179-2182.
2. C. Huang, J. Wen, Y. Shen, F. He, L. Mi, Z. Gan, J. Ma, S. Liu, H. Ma and Y. Zhang, Dissolution and homogeneous photocatalysis of polymeric carbon nitride, *Chem. Sci.*, 2018, **9**, 7912-7915.
3. T. Lu and F. Chen, Multiwfn: a multifunctional wavefunction analyzer, *J. Comput. Chem.*, 2012, **33**, 580-592.
4. Y. Wang, N. Wu, Y. Wang, H. Ma, J. Zhang, L. Xu, M. K. Albolkany and B. Liu, Graphite phase carbon nitride based membrane for selective permeation, *Nat. Commun.*, 2019, **10**, 2500.
5. L. Huang, S. Xu, Z. Wang, K. Xue, J. Su, Y. Song, S. Chen, C. Zhu, B. Z. Tang and R. Ye, Self-Reporting and Photothermally Enhanced Rapid Bacterial Killing on a Laser-Induced Graphene Mask, *ACS Nano*, 2020, **14**, 12045-12053.
6. C. Song, Z. Wang, Z. Yin, D. Xiao and D. Ma, Principles and applications of photothermal catalysis, *Chem Catal.*, 2022, **2**, 52-83.
7. Y. Zhang and M. Antonietti, Photocurrent generation by polymeric carbon nitride solids: an initial step towards a novel photovoltaic system, *Chem. Asian. J.*, 2010, **5**, 1307-1311.
8. M. Bledowski, L. Wang, A. Ramakrishnan, O. V. Khavryuchenko, V. D. Khavryuchenko, P. C. Ricci, J. Strunk, T. Cremer, C. Kolbeck and R. Beranek, Visible-light photocurrent response of TiO$_2$-polyheptazine hybrids: evidence for interfacial charge-transfer absorption, *Phys. Chem. Chem. Phys.*, 2011, **13**, 21511-21519.
9. Y. Nosaka and A. Y. Nosaka, Generation and Detection of Reactive Oxygen Species in Photocatalysis, *Chem. Rev.*, 2017, **117**, 11302-11336.
10. H. Cheng, J. Cheng, L. Wang and H. X. Xu, Reaction Pathways toward Sustainable Photosynthesis of Hydrogen Peroxide by Polymer Photocatalysts, *Chem. Mater.*, 2022, **34**, 4259-4273.
11. C. Huang, Y. Wen, J. Ma, D. Dong, Y. Shen, S. Liu, H. Ma and Y. Zhang, Unraveling fundamental active units in carbon nitride for photocatalytic oxidation reactions, *Nat. Commun.*, 2021, **12**, 320.
12. R. Cai, D. Yang, S. Peng, X. Chen, Y. Huang, Y. Liu, W. Hou, S. Yang, Z. Liu and W. Tan, Single Nanoparticle to 3D Supercage: Framing for an Artificial Enzyme System, *J. Am. Chem. Soc.*, 2015, **137**, 13957-13963.
13. J. Huang, W. Ho and X. Wang, Metal-free disinfection effects induced by graphitic carbon nitride polymers under visible light illumination, *Chem. Commun.*, 2014, **50**, 4338-4340.
14. H. F. Li, M. N. Ding, L. L. Luo, G. X. Yang, F. Y. Shi and Y. N. Huo, Nanomesh-Structured Graphitic Carbon Nitride Polymer for Effective Capture and Photocatalytic Elimination of Bacteria, *Chemcatchem*, 2020, **12**, 1334-1340.
15. S. Kang, W. Huang, L. Zhang, M. He, S. Xu, D. Sun and X. Jiang, Moderate Bacterial Etching Allows Scalable and Clean Delamination of g-C$_3$N$_4$ with Enriched Unpaired Electrons for Highly Improved Photocatalytic Water Disinfection, *ACS Appl. Mater. Interfaces*, 2018, **10**, 13796-13804.
16. H. X. Zhao, H. T. Yu, X. Quan, S. Chen, Y. B. Zhang, H. M. Zhao and H. Wang, Fabrication of atomic single layer graphitic-C$_3$N$_4$ and its high performance of photocatalytic disinfection under visible light irradiation, *Appl. Catal. B*, 2014, **152**, 46-50.
17. J. Xiao, Q. Liu, M. Song, X. Li, Q. Li and J. K. Shang, Directing photocatalytic pathway to exceedingly high antibacterial activity in water by functionalizing holey ultrathin nanosheets of graphitic carbon nitride, *Water Res.*, 2021, **198**, 117125.
18. W. J. Wang, G. Y. Li, T. C. An, D. K. L. Chan, J. C. Yu and P. K. Wong, Photocatalytic hydrogen evolution and bacterial inactivation utilizing sonochemical-synthesized g-C$_3$N$_4$/red phosphorus hybrid nanosheets as a wide-spectral-responsive photocatalyst: The role of type I band alignment, *Appl. Catal. B*, 2018, **238**, 126-135.
19. L. Ji, Y. Yan, M. Chao, M. Li, J. Gu, M. Lei, Y. Zhang, X. Wang, J. Xia, T. Chen, Y. Nie and T. Chen, Sphagnum Inspired g-C$_3$N$_4$ Nano/Microspheres with Smaller Bandgap in Heterojunction Membranes for Sunlight-Driven Water Purification, *Small*, 2021, **17**, e2007122.
20. J. Xu, Z. P. Wang and Y. F. Zhu, Highly efficient visible photocatalytic disinfection and degradation performances of microtubular nanoporous g-C$_3$N$_4$ via hierarchical construction and defects engineering, *J. Mater. Sci. Technol.*, 2020, **49**, 133-143.
21. S. F. Kang, L. Zhang, M. F. He, Y. Y. Zheng, L. F. Cui, D. Sun and B. Hu, "Alternated cooling and heating" strategy enables rapid fabrication of highly-crystalline g-C$_3$N$_4$ nanosheets for efficient photocatalytic water purification under visible light irradiation, *Carbon*, 2018, **137**, 19-30.
22. Z. Y. Teng, N. L. Yang, H. Y. Lv, S. C. Wang, M. Z. Hu, C. Y. Wang, D. Wang and G. X. Wang, Edge-Functionalized g-C$_3$N$_4$ Nanosheets as a Highly Efficient Metal-free Photocatalyst for Safe Drinking Water, *Chem*, 2019, **5**, 664-680.
23. W. Wang, J. C. Yu, D. Xia, P. K. Wong and Y. Li, Graphene and g-C$_3$N$_4$ nanosheets cowrapped elemental alpha-sulfur as a novel metal-free heterojunction photocatalyst for bacterial inactivation under visible-light, *Environ. Sci. Technol.*, 2013, **47**, 8724-8732.
24. B. Wang, Z. F. Jiang and J. C. Yu, Treated rape pollen: a metal-free visible-light-driven photocatalyst from nature for efficient water disinfection, *J. Mater. Chem. A*, 2019, **7**, 9335-9344.
25. R. Y. Miao, H. Liu, Q. Lei, L. L. Zhong, L. Zhang, J. Z. He, Z. H. Ma and Y. Yao, Single-organic component g-C$_{3.6}$N$_4$ achieves superior photoactivity antibacterial, *Chem. Eng. J.*, 2022, **440**, 135873.
26. S. L. Ma, S. H. Zhan, Y. N. Jia, Q. Shi and Q. X. Zhou, Enhanced disinfection application of Ag-modified g-C$_3$N$_4$ composite under visible light, *Appl. Catal. B*, 2016, **186**, 77-87.
27. W. J. Wang, T. C. An, G. Y. Li, D. H. Xia, H. J. Zhao, J. C. Yu and P. K. Wong, Earth-abundant Ni$_2$P/g-C$_3$N$_4$ lamellar nanohydrids for enhanced photocatalytic hydrogen evolution and bacterial inactivation under visible light irradiation, *Appl. Catal. B*, 2017, **217**, 570-580.
28. J. Dai, J. Song, Y. Qiu, J. Wei, Z. Hong, L. Li and H. Yang, Gold Nanoparticle-Decorated g-C$_3$N$_4$ Nanosheets for Controlled Generation of Reactive Oxygen Species upon 670 nm Laser Illumination, *ACS Appl. Mater. Interfaces*, 2019, **11**, 10589-10596.
29. C. Q. Li, Z. M. Sun, W. Z. Zhang, C. H. Yu and S. L. Zheng, Highly efficient g-C$_3$N$_4$/TiO$_2$/kaolinite composite with novel three-dimensional structure and enhanced visible light responding ability towards ciprofloxacin and S. aureus, *Appl. Catal. B*, 2018, **220**, 272-282.
30. J. Xu, Z. Wang and Y. Zhu, Enhanced Visible-Light-Driven Photocatalytic Disinfection Performance and Organic Pollutant Degradation Activity of Porous g-C$_3$N$_4$ Nanosheets, *ACS Appl. Mater. Interfaces*, 2017, **9**, 27727-27735.
31. P. Gao, J. Liu, D. D. Sun and W. Ng, Graphene oxide-CdS composite with high photocatalytic degradation and disinfection activities under visible light irradiation, *J. Hazard. Mater.*, 2013, **250-251**, 412-420.
32. T. Wang, Z. Jiang, T. An, G. Li, H. Zhao and P. K. Wong, Enhanced Visible-Light-Driven Photocatalytic Bacterial Inactivation by Ultrathin Carbon-Coated Magnetic Cobalt Ferrite Nanoparticles, *Environ. Sci. Technol.*, 2018, **52**, 4774-4784.
33. S. C. Hayden, N. K. Allam and M. A. El-Sayed, TiO$_2$ nanotube/CdS hybrid electrodes: extraordinary enhancement in the inactivation of Escherichia coli, *J. Am. Chem. Soc.*, 2010, **132**, 14406-14408.
34. W. Wang, Y. Yu, T. An, G. Li, H. Y. Yip, J. C. Yu and P. K. Wong, Visible-light-driven photocatalytic inactivation of E. coli K-12 by bismuth vanadate nanotubes: bactericidal performance and mechanism, *Environ. Sci. Technol.*, 2012, **46**, 4599-4606.
35. L. Noureen, Z. Xie, Y. Gao, M. Li, M. Hussain, K. Wang, L. Zhang and J. Zhu, Multifunctional Ag$_3$PO$_4$-rGO-Coated Textiles for Clean Water Production by Solar-Driven Evaporation, Photocatalysis, and Disinfection, *ACS Appl. Mater. Interfaces*, 2020, **12**, 6343-6350.
36. Z.-T. Hu, Y. N. Liang, J. Zhao, Y. Zhang, E.-H. Yang, J. Chen and T.-T. Lim, Ultra-effective integrated technologies for water disinfection with a novel 0D-2D-3D nanostructured rGO-AgNP/Bi$_2$Fe$_4$O$_9$ composite, *Appl. Catal. B*, 2018, **227**, 548-556.
37. M. Kou, Y. Wang, Y. Xu, L. Ye, Y. Huang, B. Jia, H. Li, J. Ren, Y. Deng, J. Chen, Y. Zhou, K. Lei, L. Wang, W. Liu, H. Huang and T. Ma, Molecularly Engineered Covalent Organic Frameworks for Hydrogen Peroxide Photosynthesis, *Angew. Chem. Int. Ed.*, 2022, **61**, e202200413.